HIGH FIDELITY SIMULATIONS FOR UNSTEADY FLOW THROUGH THE ORBITER LH_2 FEEDLINE FLOWLINER

Cetin C. Kiris, Dochan Kwak, William Chan and Jeffrey Housman
NASA Advanced Supercomputing Division (NAS)
NASA Ames Research Center, Moffett Field, CA 94035

Abstract
High fidelity computations were carried out to analyze the orbiter LH2 feedline flowliner. Various computational models were used to characterize the unsteady flow features in the turbopump, including the orbiter Low-Pressure-Fuel-Turbopump (LPFTP) inducer, the orbiter manifold and a test article used to represent the manifold. Unsteady flow originating from the orbiter LPFTP inducer is one of the major contributors to the high frequency cyclic loading that results in high cycle fatigue damage to the gimbal flowliners just upstream of the LPFTP. The flow fields for the orbiter manifold and representative test article are computed and analyzed for similarities and differences. An incompressible Navier-Stokes flow solver INS3D, based on the artificial compressibility method, was used to compute the flow of liquid hydrogen in each test article.

Introduction
Liquid rocket turbopumps operate under severe conditions and at very high rotational speeds. The orbiter Low-Pressure-Fuel-Turbopump (LPFTP) creates transient flow features such as reverse flows, tip clearance effects, secondary flows, vortex shedding, junction flows, and cavitation effects. Flow unsteadiness originating from the orbiter Low-Pressure-Fuel-Turbopump (LPFTP) inducer is one of the major contributors to the high frequency cyclic loading that results in high cycle fatigue damage to the gimbal flowliners just upstream of the LPFTP. The reverse flow generated at the tip of the inducer blades travels upstream and interacts with the bellows cavity. In order to characterize various aspects of the flowfield near the flowliner, various computational models have been developed and high-fidelity computations have been carried out. Results including 14 inducer rotations of a straight pipe model with the LPFTP inducer and 12 inducer rotations of the LPFTP inducer with the addition of upstream and downstream flowliners including 38 slots, an overhang area between the liners, and the bellows cavity will be reported in this paper. The incompressible Navier-Stokes flow solver based on the artificial compressibility method was used to compute the flow of liquid hydrogen in each test article. All computations included tip leakage effects with a radial tip clearance of 0.006 inches, a pump operating condition of 104.5% RPL power-level, a mass flow rate of 154.7 lbm/sec, and a rotational speed of 15,761 RPM. The findings include, a significant time-periodic back-flow generated by the inducer reaching 15-20% of the tip velocity and a jet flow of 10-15% of the inducer tip speed which penetrates into the bellows cavity creating an unsteady recirculation region in the cavity. The reverse flow and unsteady recirculation regions create an unsteady interaction between the duct and the bellows cavity resulting in high frequency cycle loading. The back-flow also creates swirl in the bellows cavity on the order of 10% of the inducer tip velocity.

Computational Models
The first computational model (**Model I**) includes the LPFTP inducer with 4 long and 4 short blades, and a straight duct, which extends 4 duct diameters upstream of the inducer. The bull nose of the inducer, and split blades are included in the model. The objective of studying the inducer model alone is to compare unsteady pressure values against existing data. To resolve the complex geometry in relative motion, an overset grid approach is employed. The geometrically complex body is decomposed into a number of simple grid components. Connectivity between neighboring grids is established by interpolation at each grid outer boundaries. Addition of new components to the system and simulation of arbitrary relative motion between multiple bodies are achieved by establishing new connectivity without disturbing the existing grids. This computational grid has 57 overset zones with 26.1 Million grid points.

The second computational grid system (**Model II**) is based on the first with the addition of the flowliner geometry. The grid system includes 38 upstream slots, 38 downstream slots, the overhang area between liners and the bellows cavity. This model is very similar to the ground test article. It consists of 264 overlapped grids with 65.9 Million grid points. Details of the grid system are shown in figure 1. The flowliner component consists of an axisymmetric chamber around the external wall of the pipe, and two rows of slots in the streamwise direction. Each slot is a rectangular shaped hole with rounded corners. On the outside wall of the chamber are the bellows which are shaped like 10 periods of a sine wave. The bellows cavity is connected to the duct via the overhang area and the slots. Two-dimensional overset grids are first created for the bellows, side walls and

the overhang area of the bellows cavity. These are then revolved 360 degrees to form the volume grids. Each slot consists of a body-conforming grid and a warped Cartesian core grid in the middle of the hole. The flowliner component alone contains 212 grids and 41 million points

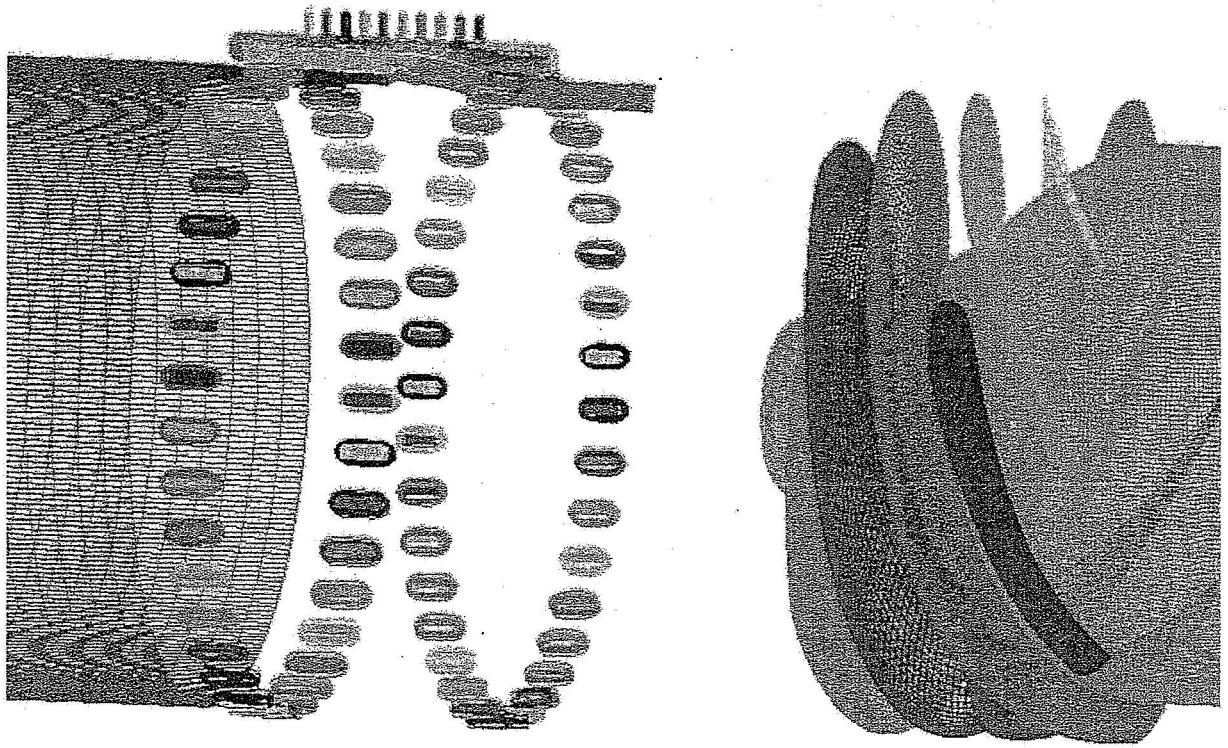

(a)

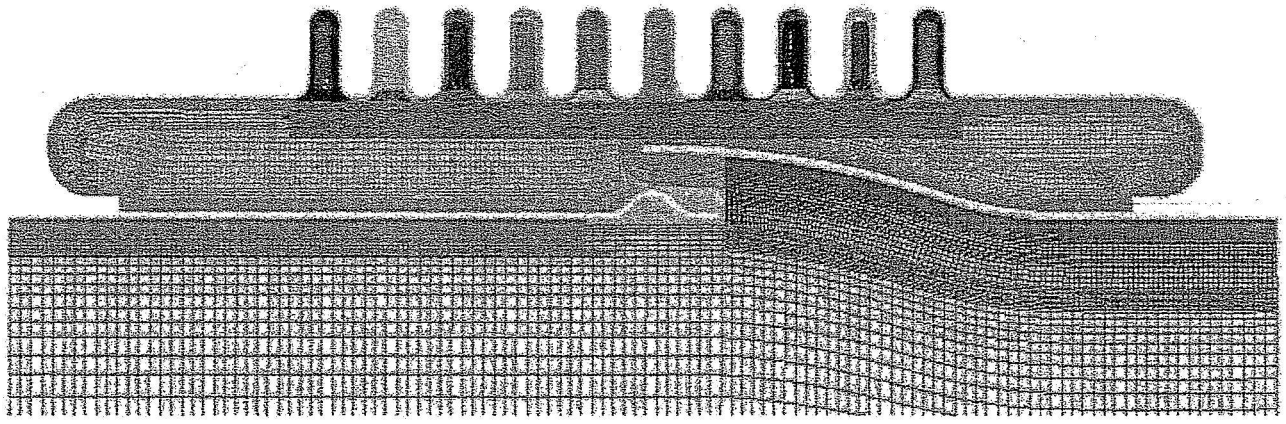

(b)

Figure 1. **(a)** Surface grids for LPFTP inducer and the Liquid LH_2 flowliner. **(b)** Details of the flowliner overset grid system.

In order to speed up and automate the grid generation procedure, a script system has been developed to automatically and rapidly perform the various steps of the grid generation process prior to the use of the flow solver. Special procedures were developed to automatically create grids for each component type. The component types included in the script are blade, pipe,

ring, nose, flowliner, and strut. The blade component is one of the most common parts of a liquid rocket subsystem and may contain multiple sections of one or more sets of different blades, e.g. inducer, impeller, diffuser. The pipe and ring components are used to connect different blade components. Pipes can be straight or curved and are bounded by the shroud. Rings can only be straight and are bounded by both the hub and the shroud. The nose component is a cap that fits at the start or end of the hub. The flowliner is a highly complex part with bellows, and slots. The strut component consists of multiple blades connected to brackets at the shroud end and a central hub at the other end. The strut component was not used in the test article, it was used in the flight configuration which was not included in this paper.

Numerical Method

The present computations are performed utilizing the INS3D computer code, which solves the incompressible Navier-Stokes equations for both steady-state and unsteady flows. The numerical solution of the incompressible Navier-Stokes equations requires special attention in order to satisfy the divergence-free constraint on the velocity field. The incompressible formulation does not explicitly yield the pressure field from an equation of state or the continuity equation. One way to avoid the difficulty of the elliptic nature of the equations is to use an artificial compressibility method, developed by Chorin[1]. The artificial compressibility method introduces a time-derivative of the pressure term into the continuity equation. This transforms the elliptic-parabolic type partial differential equations into the hyperbolic-parabolic type. An incompressible flow solver, INS3D, has been developed[2-4] based on this algorithm. Since the convective terms of the resulting equations are hyperbolic, upwind differencing can be applied to these terms. The current version uses Roe's flux-difference splitting[5]. The third and fifth-order upwind differencing used here are implementations of a class of high-accuracy flux-differencing schemes for the compressible flow equations. To obtain time-accurate solutions, the equations are iterated to convergence in pseudo-time for each physical time step until the divergence of the velocity field has been reduced below a specified tolerance value. The total number of sub-iterations required varies depending on the problem, time step size and the artificial compressibility parameter used. Typically the number ranges from 10 to 30 sub-iterations. The matrix equation is solved iteratively by using a non-factored symmetric Gauss-Seidel type line-relaxation scheme[6], which is linearly stable and allows a large pseudo-time step to be taken. Computer memory requirements for the flow solver INS3D with line-relaxation is 45 times the number of grid points in words.

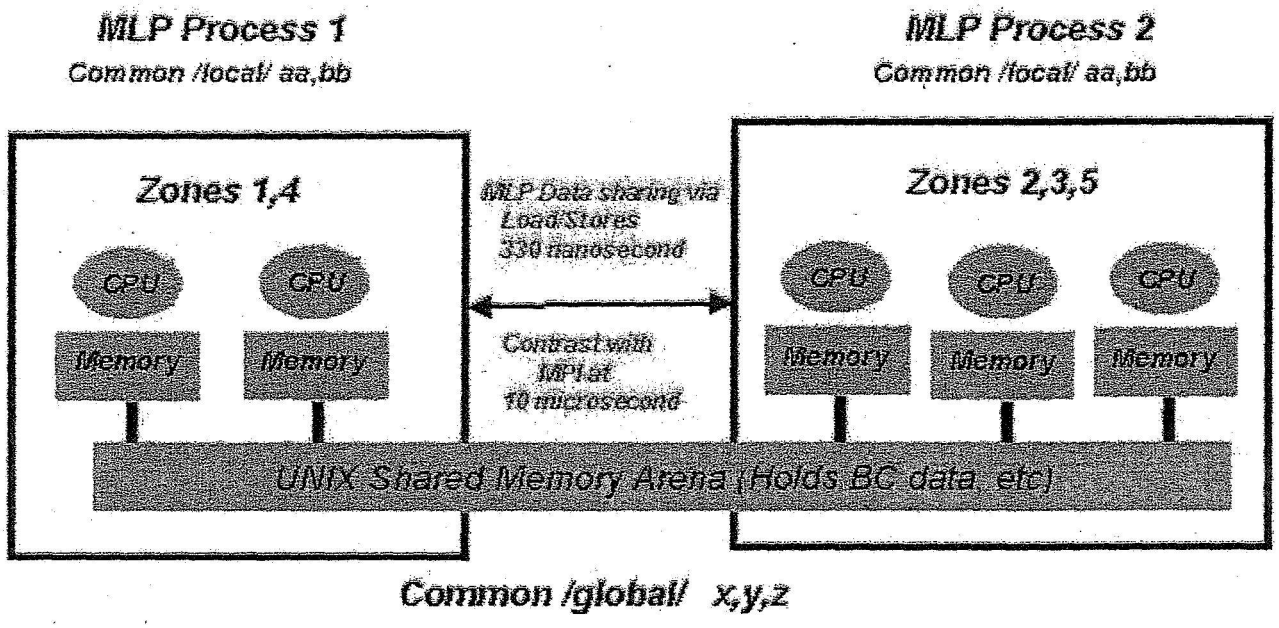

Figure 2. Shared memory MLP organization for INS3D.

Current computations have been carried out using Multi-Level Parallelism (MLP) on SGI-Origin and SGI-Altix platforms. All data communication at the coarsest and finest parallelization levels is accomplished via direct memory referencing instructions. The coarsest level parallelism is supplied by spawning off independent processes via the standard UNIX fork. A library of routines is used to initiate forks, to establish shared memory arenas, and to provide synchronization primitives. The shared memory organization for INS3D is shown in figure 2. The boundary data for the overset grid system is archived in the shared memory arena by each process. The fine-level parallelization is obtained by using OpenMP compiler directives.

Computed Results

In all computations, the inducer tip leakage effect is included with a tip clearance of 0.006 inches. The pump operating condition is 104.5% RPL power-level with a mass flow of 154.7 lbm/sec and a rotational speed of 15,761 RPM. The problem was non-dimensionalized with a reference length of one inch and inducer tip velocity. The Reynolds number for these calculations is as 36 Million. Liquid Hydrogen is treated as incompressible single phase fluid. The past decade has seen considerable progress in the development of engineering CFD models for the multiphase flows characteristic of cavitation. The most practical approach amongst these is the homogeneous-mixture model, wherein the liquid-vapor mixture is treated using individual transport equations for each phase and appropriate source terms are employed to describe the phase-change process. In spite of the progress made in multi-phase simulations in recent years, cavitation remains an extremely complex physical phenomenon. It is therefore crucial to validate these models further and obtain a confidence level before applying them to complex engineering problems.

An initial condition of flow at rest and no inducer rotation is used to start the computations. Then, the inducer is rotated at full speed as a start-up procedure. Mass flow is specified at the inflow and characteristic boundary conditions are used at the outflow. Calculations for model I and model II are currently underway. Simulations for 14 inducer rotations were competed for model I, and 12 inducer rotations were completed for model II. The history of non-dimensional pressure difference during the ninth rotation (model I) at a location where experimental measurements are taken is plotted in figure 3. Even though computed results have not fully converged to periodicity in time and may still show the evidence of start-up transients, the dominant 4N unsteadiness at a fixed location is shown in figure 3. Comparisons between CFD results and hot fire test data also show good correlation in pressure amplitude.

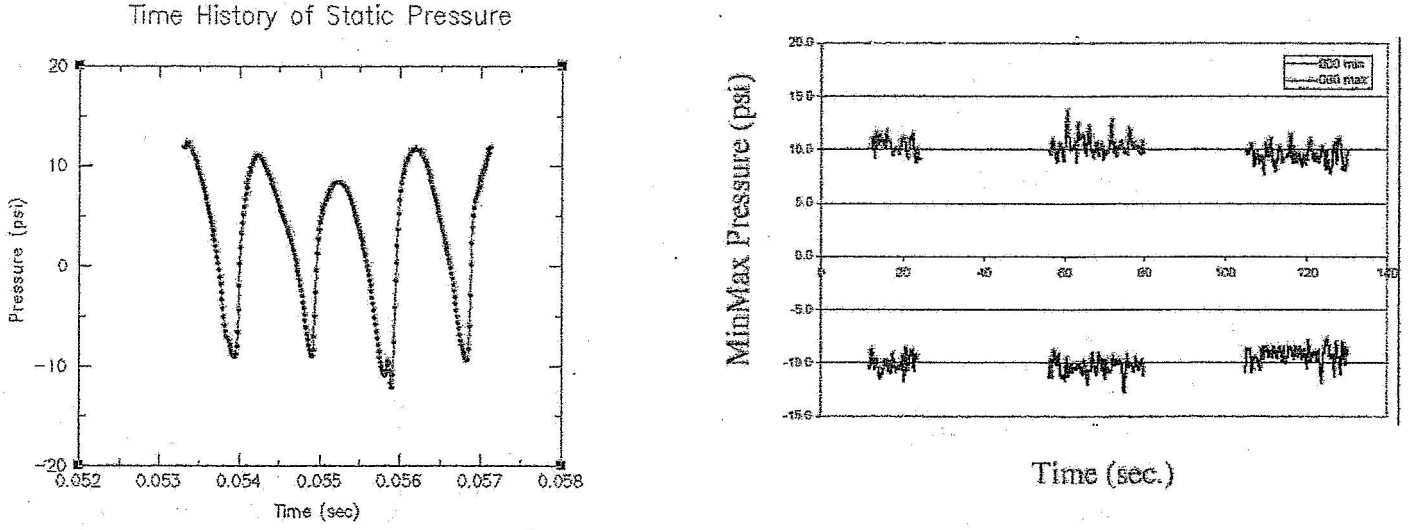

Figure 3. Time history of static pressure during one inducer rotation (model I, 14th inducer rotation), and Min/Max values of pressure in hot fire test.

Figure 4 shows the instantaneous non-dimensional pressure contours on the inducer and the flowliner surfaces (Model II). Blue color indicates the least and magenta indicates the greatest value. The pressure difference between the pressure side (facing downstream into the pump) and suction side (facing upstream) of the inducer blade is clearly seen in these pictures. The back flow near the inducer blade tip is caused by this pressure difference.

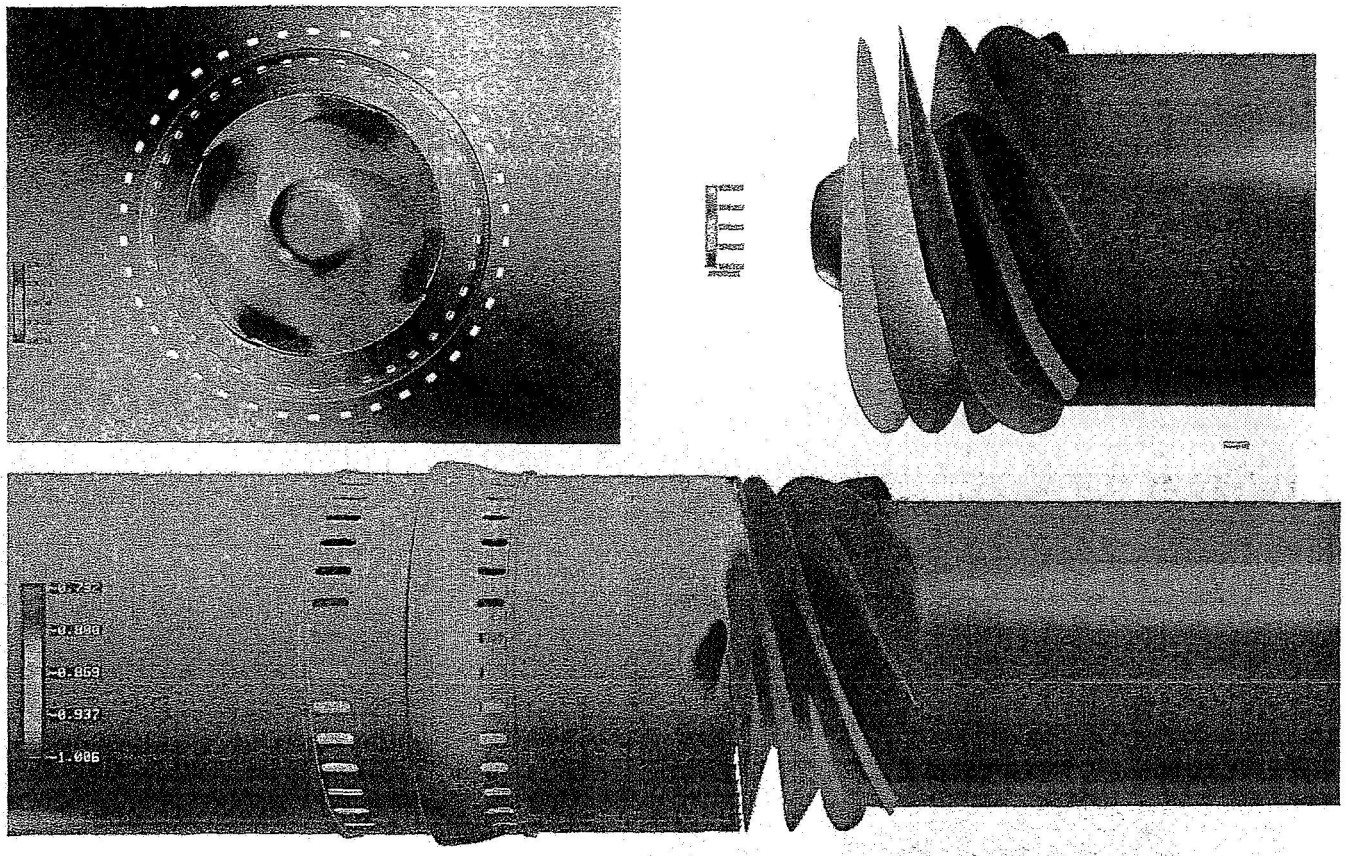

Figure 4. Instantaneous surface pressure contours on inducer and flowliner (Model II).

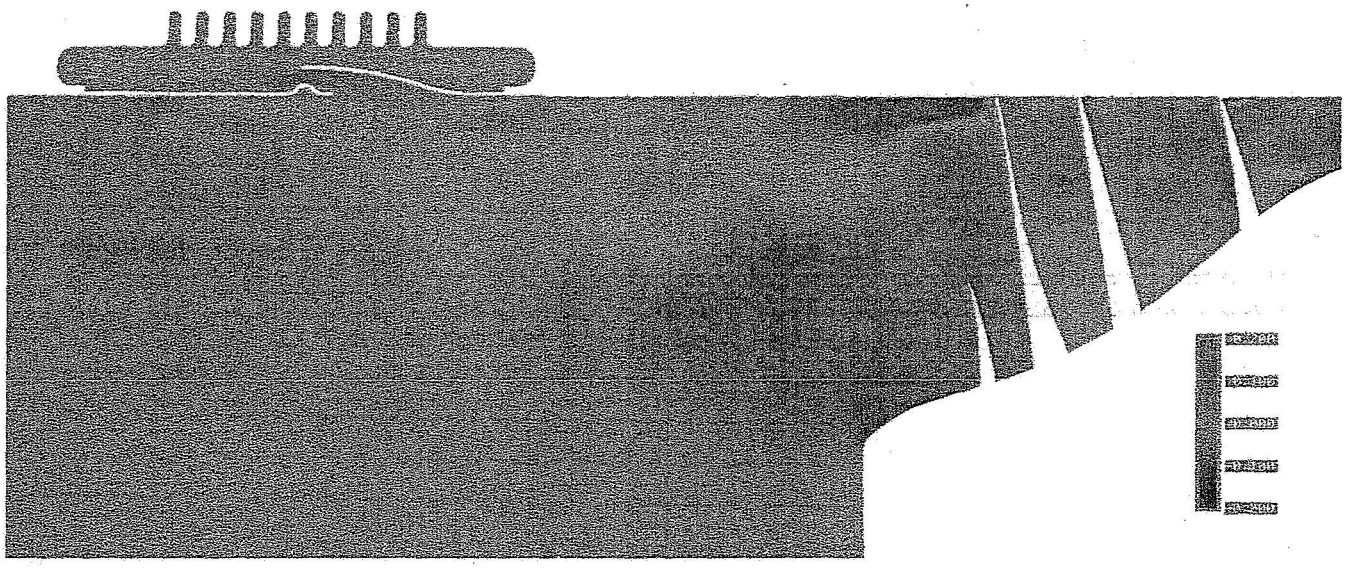

Figure 5. Axial velocity contours at an instantaneous time in a vertical cut plane.

The region of reverse flow extends far enough upstream to interfere with both flowliners in the gimbal joint. Figures 5 shows the extend of the backflow at an instantaneous time. Positive axial velocity values are colored in red and negative axial velocity values are colored in blue. Axial velocity values are non-dimensionalized by tip velocity. It is clearly seen that there is a strong interference between the backflow in the duct and the flow in the bellows cavity. The backflow velocity magnitude

reaches 15-20 % of the tip velocity magnitude in the overhang area between the liners. It should be noted that this interaction is unsteady and backflow travels in the circumferential direction as well. Due to strong interactions in the overhang area, flow is excited in the bellows area which results in time-dependent recirculation regions. This observation can be seen in figure 6, where velocity vectors are plotted in the region near bellows cavity and overhang area. As shown in figure 6, strong jet flow, with velocities of about 10-15% of the inducer tip speed, penetrates directly into the bellows cavity resulting in strong unsteady recirculation regions in the cavity. The time-dependent interaction between the duct and the bellows cavity can be one of the major contributors for high cycle loading. Figure 6 also shows that modeling the gap in the overhang area between flowliners is very important. Jet-like flow in the overhang area pushes the fluid in the bellows cavity toward the duct through slots. Without proper modeling of this detailed geometry, one can not obtain fine scale flow unsteadiness on the liner. This transient phenomena creates unsteady pressure loading spectrum on the flowliner surfaces. Backflow also causes pre-swirl to occur in the flow approaching the inducer.

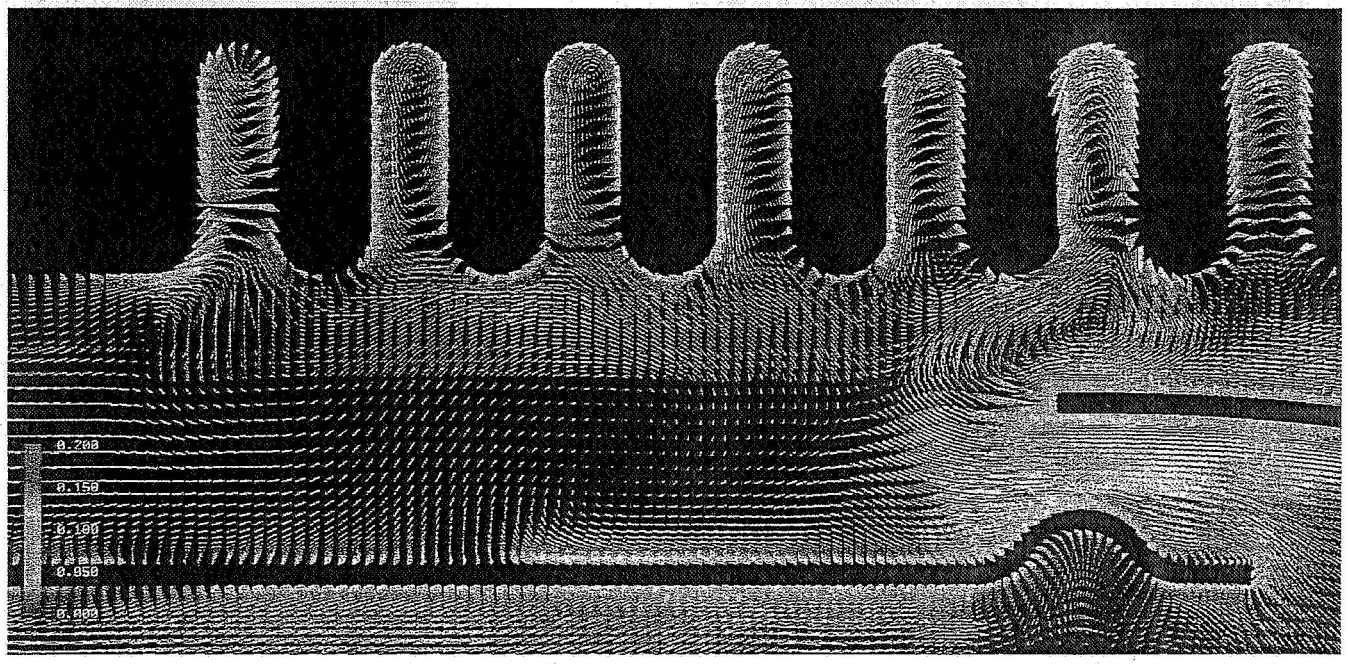

Figure 6. Velocity vectors colored by total velocity magnitude.

In figure 7a particles are released from one upstream slot, one downstream slot, and from the overhang area. In figures 7b-7d the particles are released from each of the 38 downstream slots. The mean flow direction is from left to right in the figure 7a and figure 7c, towards the inducer. In figure 7b and figure 7d we are viewing the flowliner from the inducer. The figures are snapshots from particle trace animations that have evolved for one and a half rotations. The particles are colored by the axial velocity values. The particles released from both upstream and downstream slots in figure 7a are interacting with neighboring slots traveling from the duct to the bellows cavity and from the bellows cavity to the duct. This indicates a highly unsteady interaction between the flow field in the bellows cavity and the flow field in the duct. The swirl present in the particle trace appears to be higher in the downstream slots where particles have traced four and half slots while the upstream particles have traveled only two and half slots. The particles released from the overhang area tend to travel into the bellows cavity with the exception of a few particles traveling into the duct. In figure 7b we are observing the particles from the inducers perspective where we can see the particles moving into and out of the bellows cavity through the slots. There are four regions of positive velocity particles traveling from the walls toward the center. These are particles released from the slots which do not interact with the four reverse flow regions created by the inducer. Analyzing the interior of the duct we can see the existence of the swirl near the downstream flowliner.

Examining figure 7c we can see that some of the particles released from the slots travel to the overhang region where they interact with the reverse flow and some of the particles become trapped in the bellows cavity. This suggests that some particles are recirculating through the overhang area into the bellows cavity and through the slots into the duct. This unsteady interaction between four backflow regions generated by the inducer and the secondary flow features in the bellows cavity lead to a break up of the 4theta forcing function in the flowliner area. Figure 7d suggests the existence of a 5theta forcing function, but more post-processing and future investigations should be conducted before any conclusion is made.

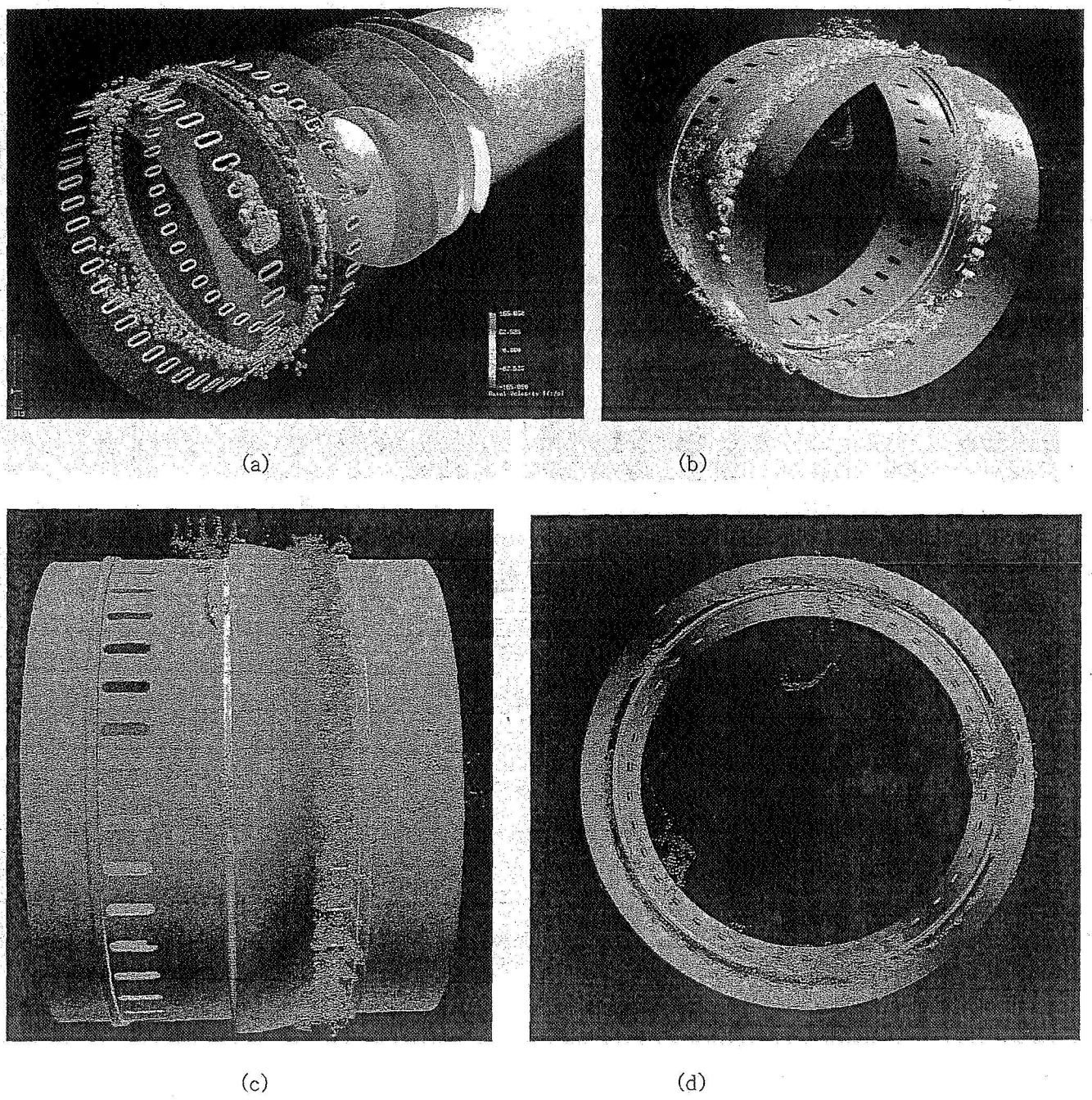

Figure 7. Instantaneous snapshots of particle traces colored by axial velocity values.

In figures 8a and 8b particles are released from the upstream slots and evolve for five inducer rotations. The color of the particles represent forward flow (blue) and backward flow (red). We see from the figures that the particles are driven towards the center of the duct and travel to the inducer where some of the particles are trapped into the backflow regions with the 4theta forcing function. In figures 8c and 8d the particles are released from the downstream slots and evolve for five rotations. In figure 8c the particles are colored the same as in the previous two figures. We observe a much more complicated flow structure where many of the particles travel into and out of the bellows cavity. In figure 8d we have multi-colored the particles with axial velocity in order to illustrate their presence in the bellows cavity. When the particles are released from the downstream slots they are under the influence of the backflow and swirl such that fewer particles travel towards the inducer.

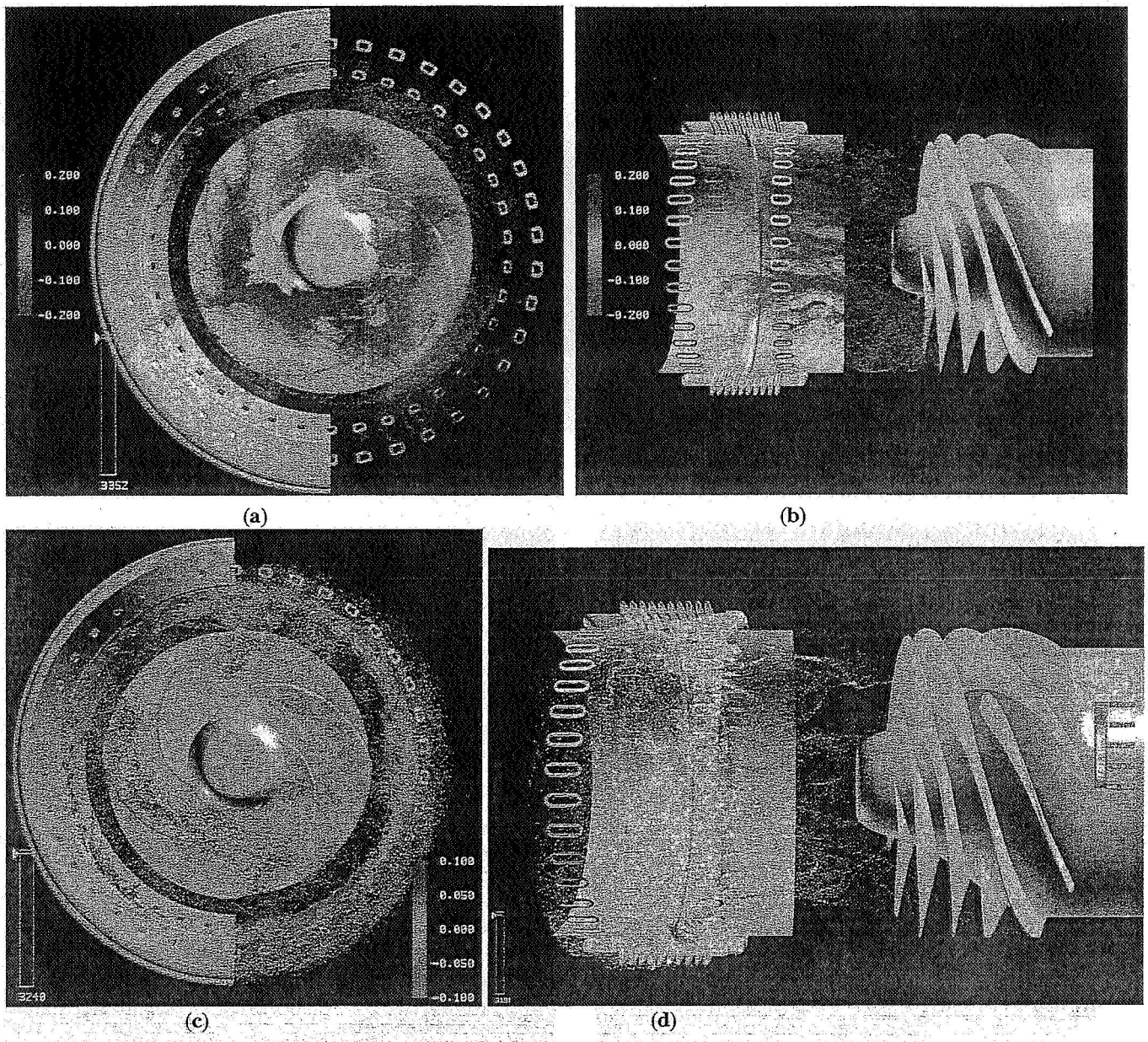

Figure 8. Instantaneous snapshots of particle traces colored by axial velocity values.

Summary

CFD results confirmed that there is a backflow caused by the LPFTP inducer. The region of reverse flow extends far enough upstream to interfere with both flowliners in the gimbal joint. Computed results for the straight duct hot fire test configuration have been verified by correlation with unsteady pressure measurements. The details of the flowfield at instantaneous times are illustrated. CFD results confirmed that there is a strong unsteady interaction between the backflow regions caused by the LPFTP inducer and secondary flow regions in the bellows cavity through the flowliner slots. It is observed that the swirl on the duct side of the downstream flowliner is stronger than on the duct side of the upstream flowliner. Due to this swirl, there are more significant unsteady flow interactions through the downstream slots than those observed in the upstream slots.

Acknowledgments

The authors are grateful to Alex Tee for his help in CAD work, and to Tim Sandstrom and David Ellsworth for their help in the visualization work.

References

1. Chorin, A., J., ``A Numerical Method for Solving Incompressible Viscous Flow Problems'' Journal of Computational Physics, Vol. 2, pp. 12-26, 1967.
2. Kiris, C., and Kwak, D., 'Parallel Unsteady Turbopump Simulations for Reusable Launch vehicle,' Frontiers of Computational Fluid Dynamics 2002, Caughey, D.A. and Hafez, M., ed, World Scientific, 2002.
3. Kiris, C., Kwak, D., and Rogers, S., ' Incompressible Navier-Stokes Solvers in Primitive Variables and Their Applications to Steady and Unsteady Flow Simulations,' Numerical Simulations of Incompressible Flows, Hafez, M., ed, World Scientific, 2003.
4. Rogers, S. E., Kwak, D. and Kiris, C., "Numerical Solution of the Incompressible Navier-Stokes Equations for Steady and Time-Dependent Problems,'' AIAA Journal, Vol. 29, No. 4, pp. 603-610, 1991.
5. Roe, P.L., "Approximate Riemann Solvers, Parameter Vectors, and Difference Schemes," J. of Comp. Phys., Vol. 43, pp. 357-372 1981.
6. MacCormack, R., W., "Current Status of Numerical Solutions of the Navier-Stokes Equations," AIAA Paper No. 85-0032, 1985.